Multi-geophysical Field Measurements to Characterize Lithological and Hydraulic Properties of a Multi-scale Karstic and Fractured Limestone Vadose Zone: Beauce Aquifer (O-ZNS)

Céline Mallet, Clara Jodry, Arnaud Isch, Gautier Laurent, Jacques Deparis, Mohamed Azaroual

Multi-geophysical field measurements to characterize lithological and hydraulic properties of a multi-scale karstic and fractured limestone vadose zone: Beauce aquifer (O-ZNS)

Céline Mallet[1] and Clara Jodry[2] and Arnaud Isch[3] and Gautier Laurent[4] and Jacques Deparis[5] and Mohamed Azaroual[6]

In : Instrumentation and Measurement Technologies for Water Cycle Management (chapter 4.8)

By Anna Di Mauro, Dr. Andrea Scozzari, Dr. Francesco Soldovieri

Abstract. The deciphering of the coupled processes that govern the transfers of mass and heat within the vadose zone is recognized as a complex issue. In this context, an observatory of transfers in the vadose zone (O-ZNS) has been implemented near Orléans (France). By combining multiscale laboratory and field experiments using various monitoring techniques, this observatory will improve our knowledge regarding water flow and contaminant transport throughout the 15-19m highly heterogeneous vadose zone. To image the lithological and hydraulic properties of its heterogeneous facies, we adopted a multi-geophysical monitoring strategy in order to overcome the limitations of each individual geophysical method. This approach includes surface, borehole, and well multi-geophysical measurements. Preliminary investigations undertaken since 2017 leads to an effective and compl ete characterization of the

[1] C. Mallet
Univ. Orléans, CNRS, BRGM, ISTO, UMR 7327, F-45071, Orléans, France
celine.mallet@univ-orleans.fr
[2] C. Jodry
Institut Terre et Environnement de Strasbourg, Université de Strasbourg/EOST/ENGEES, CNRS UMR 7063, 5 rue Descartes, Strasbourg F-67084, France
cjodry@unistra.fr
[3] A. Isch
Univ. Orléans, CNRS, BRGM, ISTO, UMR 7327, F-45071, Orléans, France
arnaud.isch@cnrs-orleans.fr
[4] G. Laurent
Univ. Orléans, CNRS, BRGM, ISTO, UMR 7327, F-45071, Orléans, France
gautier.laurent@univ-orleans.fr
[5] J. Deparis
BRGM, French Geological Survey, 45060 Orléans, France
j.deparis@brgm.fr
[6] M. Azaroual
Univ. Orléans, CNRS, BRGM, ISTO, UMR 7327, F-45071, Orléans, France
m.azaroual@brgm.fr

vadose zone including (i) a lithological description of the geological facies, (ii) the identification of local heterogeneities (karsts, fractures, silicified layers) whose density increases with depth, and (iii) an estimation of the water content variations within the vadose zone. This whole set of results constitutes a first base to ongoing joint inversion that should lead to a refined characterization of the petrophysical and transport properties of the vadose zone column.

1. O-ZNS project

1.1. Generalities

The Vadose Zone (VZ) extends between the soil surface and the water table and is of critical importance for the preservation and management of groundwater resources because of its control on transfers of water and contaminants down to the aquifer i.e. saturated zone [1,2]. Developing novel strategies for the characterization and monitoring of coupled processes at stake in the VZ is thus crucial to improving our knowledge of mass and heat transfers. However, the complexity of the heterogeneous lithologies and multi-scale structure of the VZ leaves a lot of unknowns leading to difficulties for interpreting their hydraulic and transport properties.

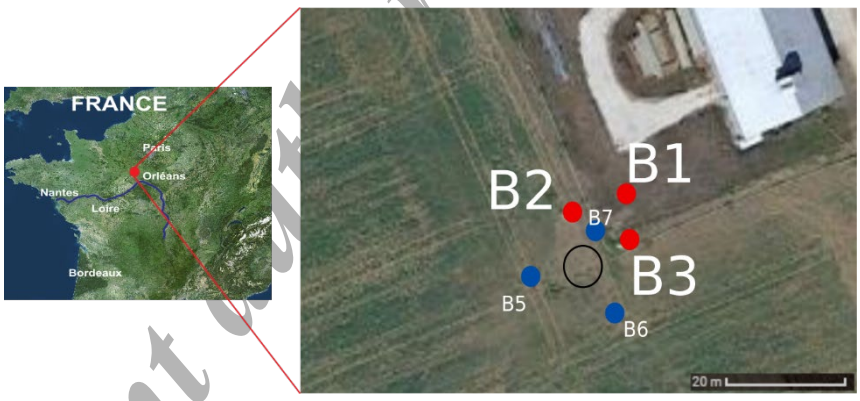

Figure 1. Localization of the O-ZNS site and its organization with the well (black circle) and the six boreholes (in red for the ones from 2017 and blue for the most recent ones from 2020) used for this study.

In this context, an Observatory of transfers in the VZ (O-ZNS) is under development within an agricultural field at the heart of the Beauce region, in Villamblain (Centre-Val de Loire, France - Figure 1 and described in Chapter II.2. by Abbar *et al* [3]). O-ZNS offers a unique support for observing and quantifying the mass and heat transfers throughout the VZ of a vulnerable limestone aquifer. This observatory is developed thanks to an exceptional well (20 m-deep and 4 m-diameter – black circle in Figure 1) and surrounding boreholes (blue and red dots in Figure 1). This configuration makes it possible to combine observations over a wide range of spatial and temporal scales. Measurements combine fo cused hydrogeological and

biogeochemical monitoring techniques together with geophysical imaging. The main objectives, the localization, borehole details, and the instrumentation strategy of the O-ZNS platform are presented in a companion chapter [3]. For this study, we mainly consider three cored boreholes (B1 to B3 in red in Figure 1) drilled in spring 2017. Newer boreholes, drilled in spring 2020 and denoted B5 to B7 (displayed in blue in Figure 1), are also shown and used for direct log imagery.

1.2. HydroGeophysical approach for subsoil characterization

Geophysical methods have been developed for characterizing underground microstructural, petrophysical, and transport properties, including karst properties, within the VZ [4]. Considered individually, these methods have specific limitations in terms of resolution and depth of observation but they also have their specific interest. For example, surface-based seismic methods are adapted to detecting horizontal objects [5], electrical method to characterizing fluid saturation and behavior [6], electromagnetic methods for identifying karst and factures, and inferring water content [7,8], microgravimetric methods to detect deeper heterogeneities that could be hydrogeological anomalies and to estimating water storage [9].
Coupled geophysical approaches and joint inversion have been developed to broaden physical description, range of resolution, and depth of observation [10-12]. For example, fracture density characterization is enhanced by coupling seismic and electric methods [13]; aquifer storages are better monitored when crossing gravimetric and electromagnetism [14]; seismic characterization of shear zone is much more accurate when coupled to electromagnetism [15]. More recent approaches couple geomechanical, geological, and geophysical data to improve models and recover meaningful hydrological and reservoir properties at various scales [16-19]. However, these methods, while based on model development, are still needing experimental laboratory and field validations [13,20-21]. Improvements are still underway to balance the uncertainties between each field and those related to the petrophysical relationships linking geophysical and hydrological quantities [22-25].

There are recent large-scale field hydro-thermo-geophysical experiments that tested coupling models and push forward our knowledge on subsoil characterization and on fluid flow within the VZ [26-30]. These studies, performed under more or less controlled conditions and more or less blind soil structure, highlighted the importance of being able to couple field hydraulic experiments to geophysical field and laboratory characterization. It is in this lineage that O-

ZNS takes place. Indeed, the challenge posed by the characterization of the hydraulic and transport properties of the VZ calls for a coupled multi-geophysical approach. It will provide a multi-scale characterization of the VZ facies in the context of highly heterogeneous lithological and hydraulic properties [31]. In addition, it is expected to provide exceptional study outlooks with time monitoring, coupled measurements and joined interpretations and inversions. The full and specific O-ZNS geophysical strategy based on the state-of-the-art applied to a VZ of a limestone aquifer is presented in Section 2, following the lithology and structure description.

1.3. Overall lithology

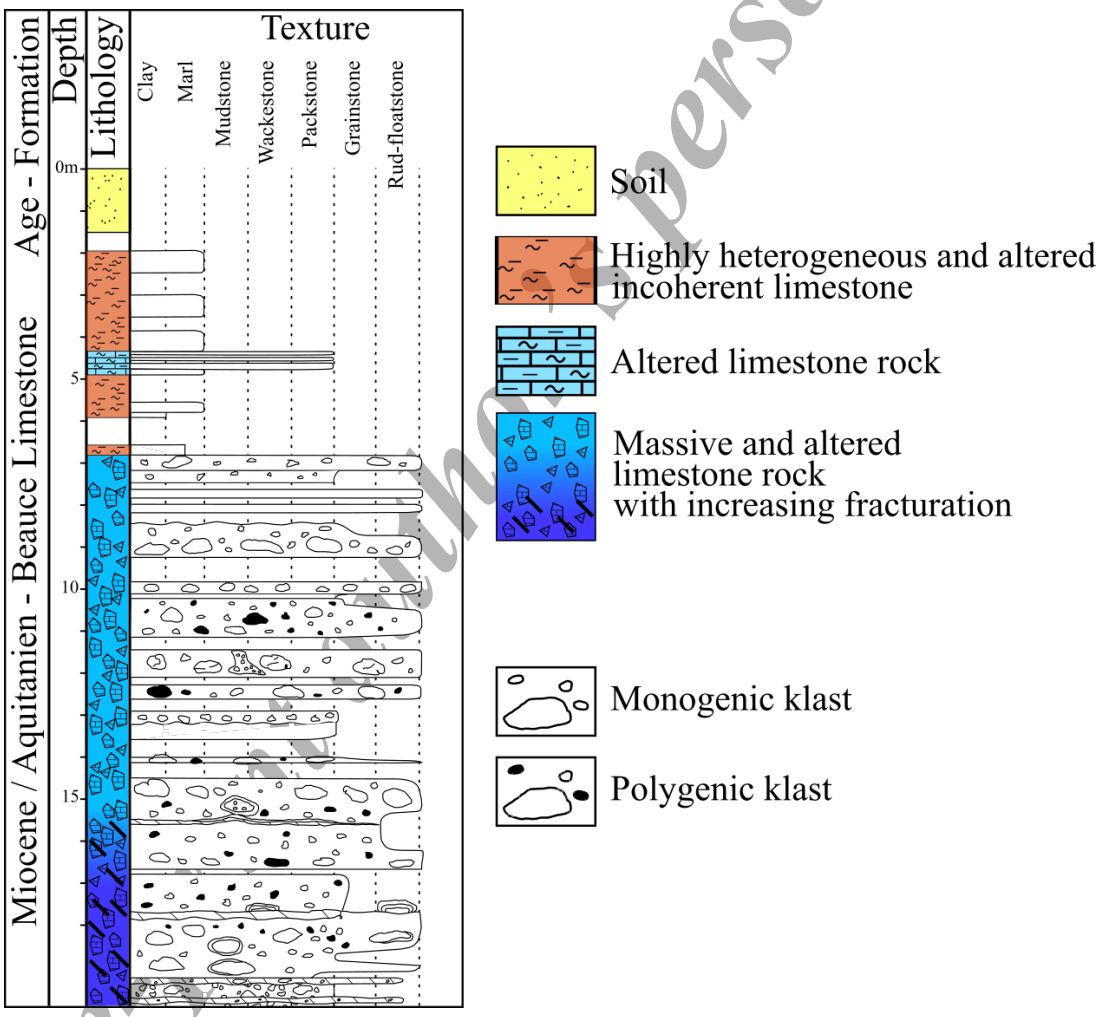

Figure 2. Lithology of the VZ interpreted from direct core observations and log imagery in six boreholes (B1-3 and B5-7)

In this section and the following, a description of the VZ facies and the site heterogeneities are presented giving a general view of the geological structure. The lithological description of the Beauce limestone aquifer is displayed on Figure 2. It has been depicted from direct core observations taken from B1-3 [31] and complemented with log imagery from B5-7 boreholes.

The global formation presents a heterogeneous altered/karstified li mestone facies, with a macro- and micro-porosity, cracks and fractures.

From the surface down to 25 m deep, the following facies identified as part of the Pithiviers limestone formation were observed:

- 0-1.5 m: silt loam soil typical of the Beauce region [32].
- 1.5-7 m: highly heterogeneous incoherent limestone presenting intense alteration (i.e., fractures, weathering, oxidations), powdery limestones, clay lenses, calcareous sand interbeds, and few thin massive, but still altered and karstified, limestone facies (the blue altered limestone rock displayed on the log in Figure 2).
- 7-20 m: massive and altered limestone rock presenting heterogeneous fracture density (especially after 15 m deep).
- 20-25 m: interbeds of silicified limestone and pluri-centimetric silica cherts. Some rare silicified zones are observed in the previous layers (below 18 m deep) but not recurrently thus not appearing in the log.

The whole column is developed on a semi-permeable layer of white clay that was identified as part of the *"Molasses du Gâtinais". The bottom of this layer has not been reached by the boreholes* but its thickness regionally ranges from 1 to 2 m.

The water table level is not depicted on the lithological log. It usually varies between 18 and 20 m deep, with historical variations from 14.5 to 22.5 m deep [31,33]. For each of the result presented in this paper, the depth of the water table was measured from the O-ZNS boreholes and is presented in the corresponding section.

1.4. Geological structures characterization

Optical log imaging (May 2020, B5 to 7, Figure 3) provide a clear view of the largest heterogeneities (dm to m scale) that can be found along the VZ of the O-ZNS experimental site. Different types of porosity (cracks, pores, fractures, karsts) are observed in the limestone rock facies with an increasing occurrence of karstification and fracturation with depth.

Drill core pictures (Figure 4A) and 3D reconstruction by photogrammetry of a core sample (Figure 4B) illustrate the complex and multi-scale (mm to cm) smaller heterogeneities such as macro-pores, clasts, and cracks. Figure 4A also illustrates the facies described in Section 1.2 with first, the soil, followed by the highly heterogeneous incoherent limestone (with a thin layer of massive limestone) and the limestone rock, more or less altered and fractured.

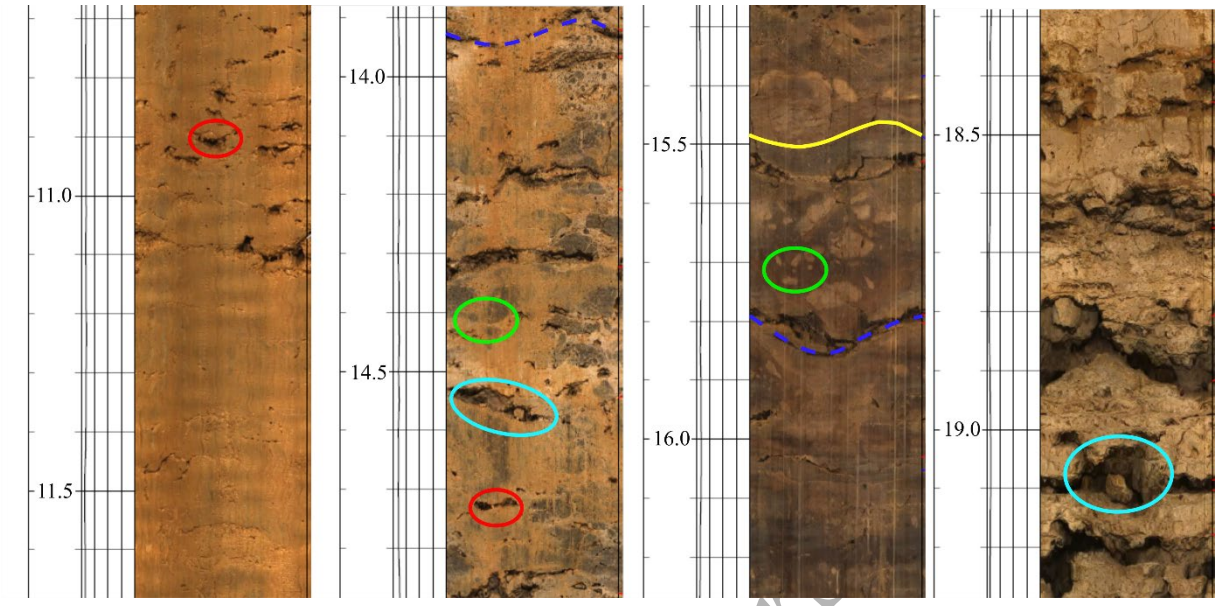

Figure 3. Imagery of B5 at different depths highlighting the variety of heterogeneities (macro-pores in red, clasts in green, macro-cracks/fractures in dark blue, karsts in light blue, lithological interfaces in yellow).

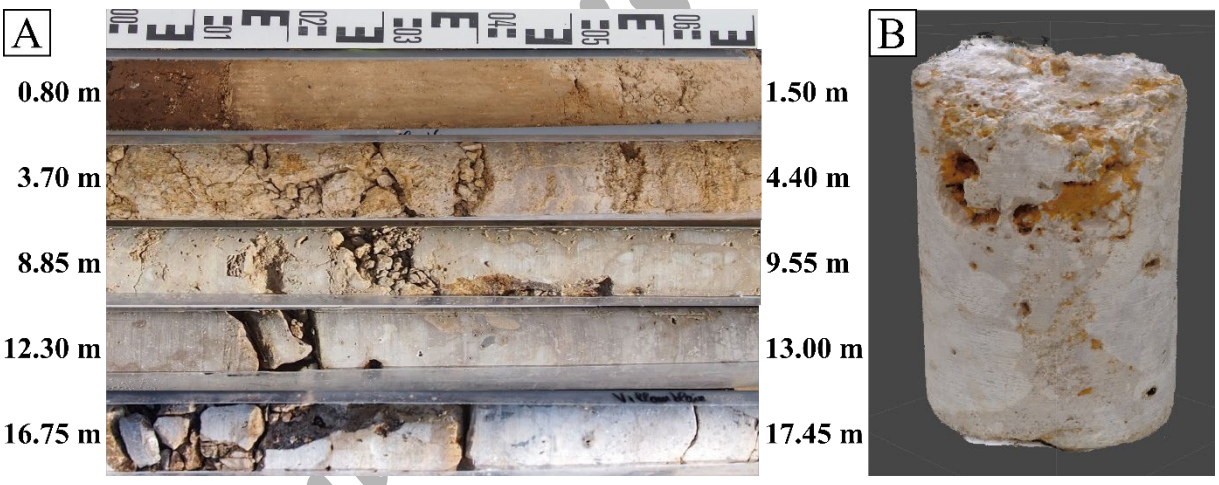

Figure 4. A) Pictures of cores from B1 (70 cm each) taken in the four facies presented in Figure 2. B) 3D reconstruction of a core sample taken from B7 at 11 m deep.

At a lower scale, Figure 5A presents optical microscopic views of massive limestone rock taken between 11 and 14 m deep. We observe mechanical and chemical micro-heterogeneities as cracks developing inside grains (intragranular cracks), oxidation and dissolution-recrystallisation of the calcite [26]. The lowest scale of scanning electron microscopy (SEM) highlights the micro porosities (Figure 5B).

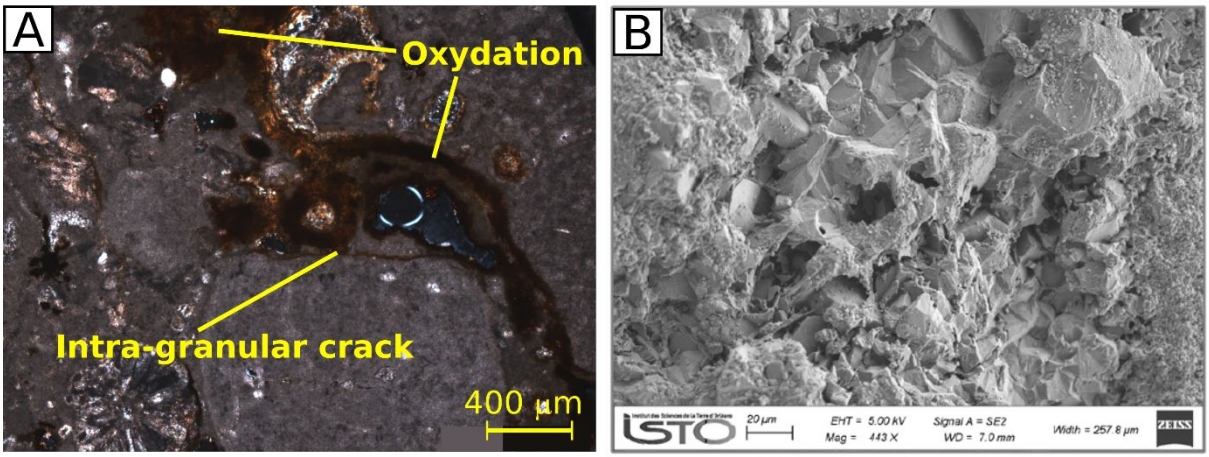

Figure 5. A) SEM observation of micro-porosity in limestone rock from B2 at 9.7 m deep. B) Polarized microscopic observation of calcareous matrix showing oxidation and intra-granular crack, from B2 at 11.1 m deep. Modified from [34].

To summary the multi-heterogeneities, Table 1 gives their ranges of length and aperture measured following a vectorization method [35-36] and observed on these figures and in the whole work of Aldana [34]. Note that for the fractures the upper size is yet unknown and will be determined with future field imagery investigations.

Table 1. Classification of heterogeneities observed on log imageries, core samples (as in Figure 4) and microscopic observations (Figure 5 and [37]).

	Length		Aperture	
	min	max	min	max
Spherical pore or clast	5 µm	60 mm		
Crack	1 mm	10 cm	1 µm	6 mm
Fracture	10 cm	unknown	> cm	unknown
Karst	5 cm	30 cm	1 cm	5 cm

2. O-ZNS geophysical strategy

2.1. Interest of a multi-geophysical approach

As introduced in Section 1.2, coupling geophysical methods broadens the physical description, the range of resolution and depth of observations, as suggested by Figure 6 which presents all methods used during O-ZNS preliminary investigations.

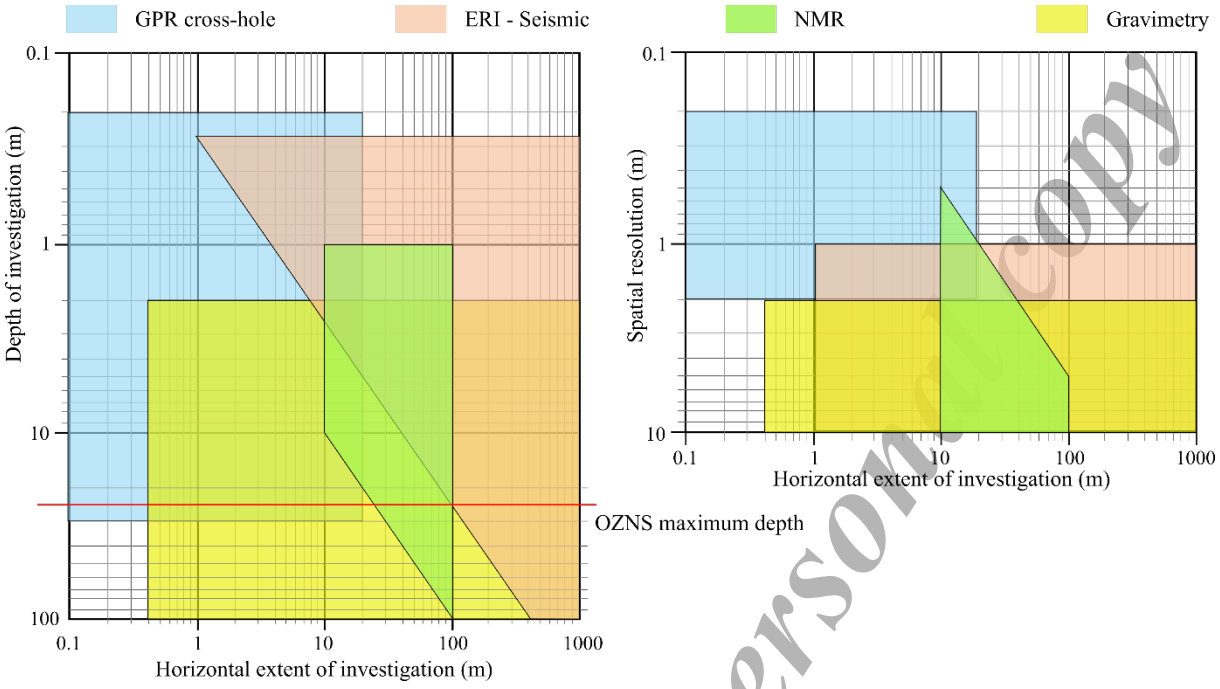

Figure 6. Comparison of depth of investigation and spatial resolution of geophysical methods: GPR, ERI, Seismic, NMR, and Gravimetry. Adapted from Fan et al. [36], authors' experiences and other synthetized data (e.g. [37]).

Specific advantages and drawbacks of the four methods used for this study are detailed below:

- Nuclear Magnetic Resonance (NMR) monitors the electromagnetic signal produced by water bodies in response to oscillating magnetic perturbations [40-41]. As this method directly relates to the water content, it is primarily used to estimate hydraulic properties of the VZ [40]. NMR also provides different scales of observation with surface (SNMR or MRS [7]), borehole, and recently, surface-to-borehole measurements [41-42]. Development of multi-channel instruments has also allowed to access from 1D to 2D and 3D measurements [43]. Although the poor signal to noise ratio limits this method [42], it has proven its efficiency for limestone VZ and karstic aquifer characterization [7,45-46]
- Seismic refraction methods [47-49] are best applied to the characterization of tabular objects such as soil layers or horizontal cracks [5]. They also provide insights into water saturation for groundwater modeling [47] or into deep formations [39]. Seismic interpretation can be complex, even unsolvable when crossing blind zone (i.e. velocity decrease in function of depth) [48]. However, as saturation increases P and S-wave anisotropy [49], it may allow to better characterize the presence of fluid.
- Electromagnetic methods [6,50] such as DC Electrical Resistivity Imaging (ERI) [51] and Ground Penetrating Radar (GPR) [50, 52-53] depend on many factors, including salinity, water content, cation exchange capacity and porosity of the material [54-55]. Although

these methods can be applied to the monitoring of the water content, for example in agriculture [56] and the VZ of calcareous environments [57], the interpretation of direct current resistivity data alone is particularly complex because it is often impossible to separate the so-called volume contribution from that of the phase interfaces (conduction of electrical double layer) [58]. While GPR gives high resolution, in conductive environment, it presents a small penetration depth [59]. Since these two methods (ERI and GPR) have complementary resolution, they are often coupled together [60].

2.2. Overview of the measurements made on O-ZNS experimental site

Surface measurements

The area around the O-ZNS experimental field has been historically studied with early observation conducted by INRAE and BRGM since the 1990s [7,32,56] and more recently by ISTO as part of several projects. From that time, electrical map and electrical resistivity tomography have been made together with SNMR measurements (monitoring 1999-2000 and 2017) on a field located in close proximity (1 km south) of O-ZNS experimental site [7].

Since the beginning of O-ZNS project surface investigations have been conducted including:

- 1D and 2D SNMR in January 2019.
- 2D ERI in 2017, 2018 and 3D in April 2019.
- 2D seismic in October 2018.

Finally, in August 2020 a multi-geophysical monitoring campaign has been carried out that included 2D seismic surface, 3D ERI, 3D SNMR and gravimetry mapping. These full data sets, coupled to the borehole measurements performed at the same time (Table 2) will be joined in a global inversion for future contribution and will complement the initial characterization of the VZ functioning undertaken since 2017.

Borehole measurements

In addition to surface measurements, the same methods have been employed in boreholes when applicable (Table 2). Note that due to wave attenuation (i.e. high conductive subsurface zone), GPR measurements are only feasible in borehole and cross-hole fashion.

Future equipment and measurements

The instrumentation strategy of the O-ZNS project is briefly detailed in the Chapter II.2. by Abbar *et al* [3] with the description of few hydrogeological monitoring solutions under consideration and the installation of fiber optic sensors. Indeed, continuous measurements are

planned for monitoring purposes, including three distributed fiber optic sensors (temperature-DTS), strain-DSS and acoustic-DAS) installed in a continuous and permanent loop along B5, 6 and 7 boreholes. In addition, in the same boreholes, seismic and GPR monitoring are planned as well as the implementation of vertical electrical resistivity devices to continuously monitor the conductivity of the VZ materials.

Further geophysical equipment are expected once the well is in place: seismic measurements, composed by 60 triple geophones with a natural frequency of 100 Hz and a seismic well source; GPR antennas placed on the inside on the well to communicate with the surrounding boreholes; gravimetry and muon measurements from inside the well. From the wall of the well itself, lateral slanted boreholes will be drilled at various depths containing further geophysical equipment such as Time Domain Reflectivity (TDR) probes (communicating with surface probes and GPR antenna fixed in the lateral wall) to measure permittivity, polarizable and unpolarizable electrodes for DC electrical resistivity and spontaneous potential measurements respectively.

Table 2. Borehole measurements on O-ZNS experimental site. B4 and 8-9 are presented in Abbar et al. (Chapter II.2. – [3])

Method	Borehole	Date	Made with	
Log	B1 to 4	03-2017	Iduna-Soleo	Diameter, electric conductivity, γ-γ
Log	B1 to 4	03-2017	Iduna-Soleo	Diameter, trajectory, imaging (low resolution), γ-ray
Log	B1 to 4	05-2017	Iduna-Soleo	Neutron-neutron
GPR	B1 to 3	01-2019	BRGM-EOST	Cross-hole: 3 panels
Log	B5 to 9	05-2020	Semm Logging	Diameter, electric conductivity, trajectory, imaging, γ-γ, neutron-neutron, γ-ray
GPR	B5 to 8	08-2020	BRGM	Borehole and cross-hole (6 panels)
Log	B6 to 7	09-2020	Semm Logging	γ-γ, neutron-neutron (cased hole)
Log	B5 to 8	09-2020	NMRSA	NMR
Log	B5 to 8	09-2020	Geosciences Montpellier	γ-ray, magnetic susceptibility, electric conductivity, physico-chemical parameters (pT, Eh, pH), PS in a single borehole
Seismic	B5 to 8	10-2020	BRGM	Cross-hole (P and S-wave)

2.3. Protocols of the measurements presented in this study

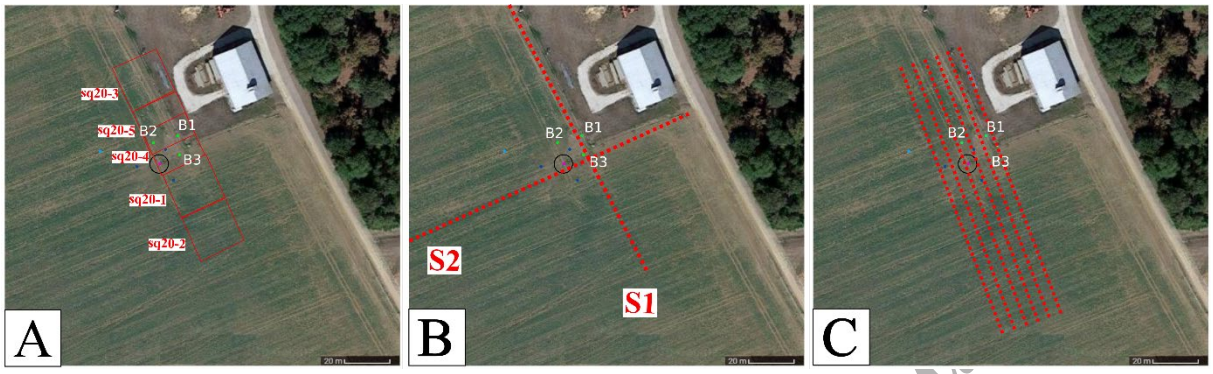

Figure 7. Surface field measurements presented in this study. A) NMR loops of Jan. 2019. B) Seismic lines of Oct. 2018. C) Electric lines of Apr. 2019.

Even though all scales of NMR survey are applied at O-ZNS site, this chapter focusses on a **Surface Nuclear Magnetic Resonance (SNMR) survey**, performed in January 2019, which consisted in four soundings aligned in half-over lapping square loops along a North-West profile using coincident transmitter and receiver loops (Figure 7A). The loops are of 20 m x 20 m side with two turns to concentrate our investigation on the superficial part of the aquifer. Thanks to the multi-channel NMR system NumisPoly®, a synchronous reference loop was placed nearby to mitigate the noise. Indeed, this loop was placed far enough to avoid the NMR signal and close enough to register the same ambient electromagnetic field as the measure loop. Note that a preliminary measurement using a pair of eight-shape loops [44] proved the O-ZNS site to have low level of noise.

The pulse frequency was 2034 Hz according to the Larmor Frequency, which is the precession of the magnetic moment, in Central France at the date of measurements (January 2019). Each sample contains 200 records (commonly called stacks) of 24 ms length sampled at 19.2 kHz and include a band-pass (16 Hz) and Notch filter. The measurements comprised 10 pulses with a maximum pulse moment of 3.500 A-ms.

The post-processing is based on previous analyses defining ambient noise between 100 and 200 nV [61]. The NMR inversion has been done thanks to SAMOVAR® software based on the Tikhonov regularization method [40] and resistivity of the subsurface obtained by the ERI inversions (see below).

Surface seismic measurements performed in October 2018, consisted in two lines (S1 and S2) measuring P-wave velocity and crossing the O-ZNS site (Figure 7B). The two perpendicular lines of 144 m were equipped by Z-component geophones (with natural frequency of 14 Hz)

spaced by 1 m. According to the profile length, this spacing ensures a depth of observation up to the limestone rock located at 20 m deep. The shots were made by a 5 kg hammer every 4 geophones starting at 0.5 m after the first geophone, for both lines. The first arrival times were inversed using RAYFRACT® software [62-63] in order to obtain 2D spatial variations of P-wave velocity. During inversion process, the Eikonal equation is solved numerically by a finite difference method approach [64-65].

Electrical Resistivity Imaging (ERI) performed in April 2019 consisted in a direct 3D acquisition of 288 electrodes. Specifically, it is composed by six linked 3D profiles made of 48 electrodes with an electrode spacing of 2.5 m and an inter-line spacing of 5 m thus covering a total area of 117.5 m x 25 m. Acquisition was carried out with a Syscal Pro® using two configurations. The first one has 7,574 quadrupoles of dipole-dipole type. The second configuration is composed of 5,130 gradient-type quadrupoles. Both include x1 quadrupoles for each line and x2 inter-line quadrupoles. The measurement sequences include electrical resistivity as well as induced polarization. The same parameters have been applied to each configuration and comprise an injection time of 2,000 ms, semi-log chargeability sampling (not shown here), a standard deviation of 5 % on 3 to 10 stacks and requested injection and reception voltage of 50 mV to 800 mV respectively. Finally, both datasets were merged and processed (filter on reception voltage) to obtain a number of 9,295 inverted measurements. Inversion of apparent resistivity values used BERT software [66] with a lambda regularization equal to 20, a L-curve optimization and with L1 norm (robust inversion). The model grids contain 83,866 cells and inverse model contain 44,510 cells. After 6 iterations, the Chi^2 value is equal to 1.50 and 1.46 and the Root Mean Square (RMS) is equal to 5.46 % and 0.21 % respectively for Resistivity and IP measurements.

The **Ground Penetrating Radar (GPR)** was performed in January 2019, and acquired with a ProEx GPR system (Malå Geosciences). We used Malå 100 MHz borehole antennae, with a sampling frequency of 1,000 MHz and time-window of 240 ns. All measurements were stacked 128 times. Acquisition consists in 3 Zero Offset Profile (ZOP) between B1-2; B2-3; and B3-1. The ZOP profiles can be thoroughly investigated as providing a 1D log view as depth between each borehole. ZOP profiles consist in simultaneously descending the transmitting antenna and the receiving antenna in two different boreholes. The measurement step is equal to 50 cm. The

data were processed using a zero phase 40-180 MHz band-pass filter with an Automatic Gain Control (AGC) time equalization. It is used only for picking first arrival. A final stage consists in picking of the first arrivals. Knowing the distance between two boreholes, the picking of the first arrival was transformed in apparent relative permittivity (ε_r) [67].

3. O-ZNS preliminary characterization

3.1. Surface results

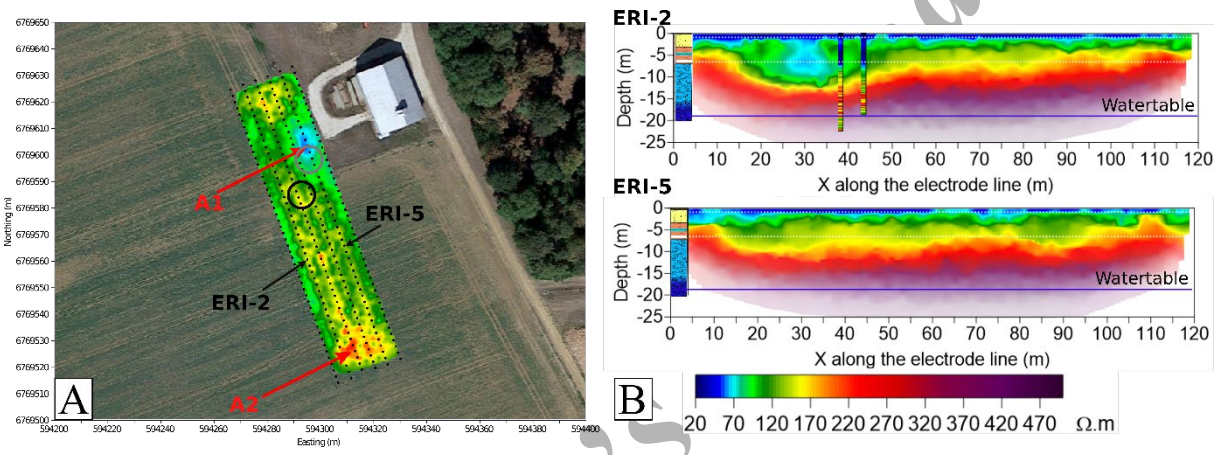

Figure 8. A) Electric resistivity observed on the 2D surface at 5 m-deep. Black and grey circles are the O-ZNS well localization and the initially planned one, respectively. B) ERI-2 and ERI-5 profiles. On ERI-2 profile, B3 and B4 (a pressiometric borehole, located in the middle of B1, 2, 3 and presented in Abbar et al. - Chapter II.2. – [3]) are shown [68]. Resistivity scale is for both figures. The water table level is indicated from our piezometric data at the date of the ERI measurement.

Figure 8A presents resistivity issued from the 3D electrical survey at 5 m deep. Resistivity map highlights two different anomalies with lower (A1) and higher (A2) resistivity than background. Considering that at 5 m deep, we are in the strongly altered limestone layer, the A1 anomaly is considered here as an incoherent limestone with high content of clay while A2 anomaly is assimilated to calcareous sand or altered limestone rock with low content of clay. Initially, O-ZNS main well was supposed to be located on the A1 heterogeneity (cf., grey circle on Figure 8A). Following this first characterization, the well has been moved to the black circle in order to include this area in the monitoring as well as the representative background area.

Note that due to resolution limitations of the method, we are not sensitive to the apparition of the water table. Indeed, in the presence of water, resistivity should decrease. The fact that a decrease in resistivity value was not observed is due to our field protocol and inversion process that put forward the first ten meters instead of deepest points. The idea of this first

characterization is indeed to accurately describe the spatial variations between the surface and 10 m-deep.

3.2. 2D profiles

ERI-2 and ERI-5 profiles depicted on Figure 8A, also taken from the 3D ERI, are shown on Figure 8B. ERI-2 profile further illustrate A1 heterogeneity. Indeed, it goes from the sub-surface (around 1-2 m deep) to 12 m deep. Both profiles recover the three main geological facies identified on the core samples during the lithological description, at a lower resolution but at a larger scale. The first layer of soil (0-1.5 m deep) presents an electric resistivity of 20 Ω.m. It is followed by the heterogeneous altered limestone facies, from 2 to 7 m deep, with an electric resistivity around 120 Ω.m apart from A1 patch. Under this depth, the electric resistivity increases up to 500 Ω.m down to 25 m deep. Chargeability is not shown here, but locally, the A1 heterogeneity goes up to almost 6 mV/V [68]. Due to this higher chargeability, we confirm that this layer and the A1 anomaly are filled by clayed materials.

Figure 9 introduces S1 and S2 profiles (Figure 7B) and their respective P-waves velocities obtained in October 2018. Again, these surface measurements confirm the three facies succession with values under 500 m/s for the silt loam soil, from 500 to 1,200 m/s for the altered limestone facies between 1.5 and 7 m deep, and an increasing velocity up to 3,500 m/s for the massive and altered limestone rock. Apart from that, this investigation was not able to detect any other feature. Note that raw data showed high discrepancy and anisotropy for the altered limestone facies that have been smoothed out here by the inversion process.

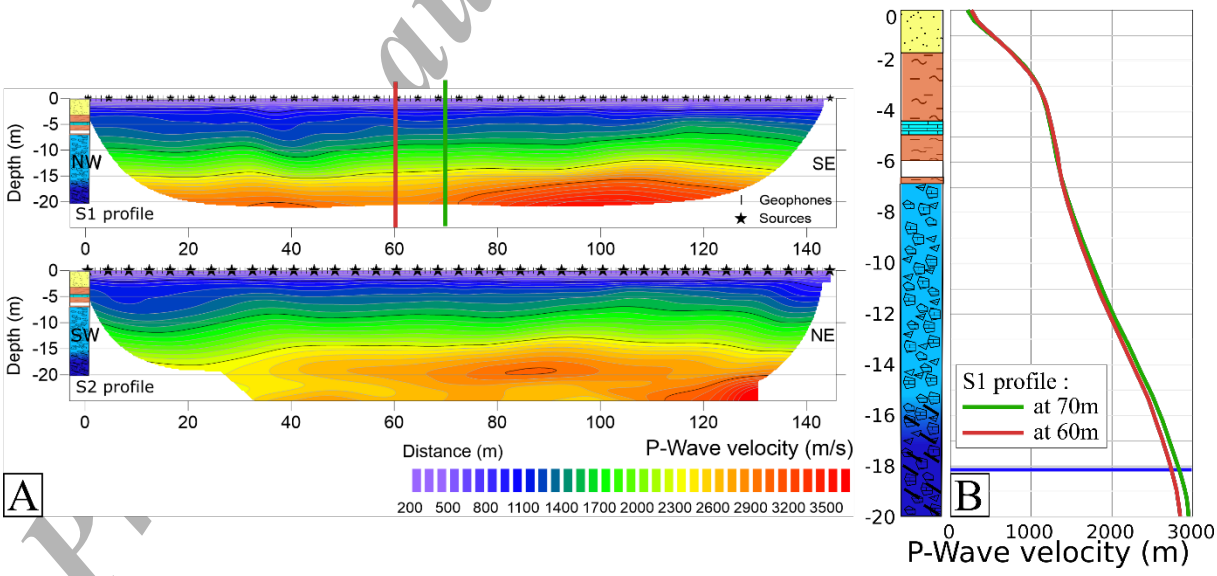

Figure 9. A. P-wave velocities obtained on both seismic profiles made in October 2018. B. Two vertical velocity log extracted from S1 profile (lithologic log are recalled along depth).

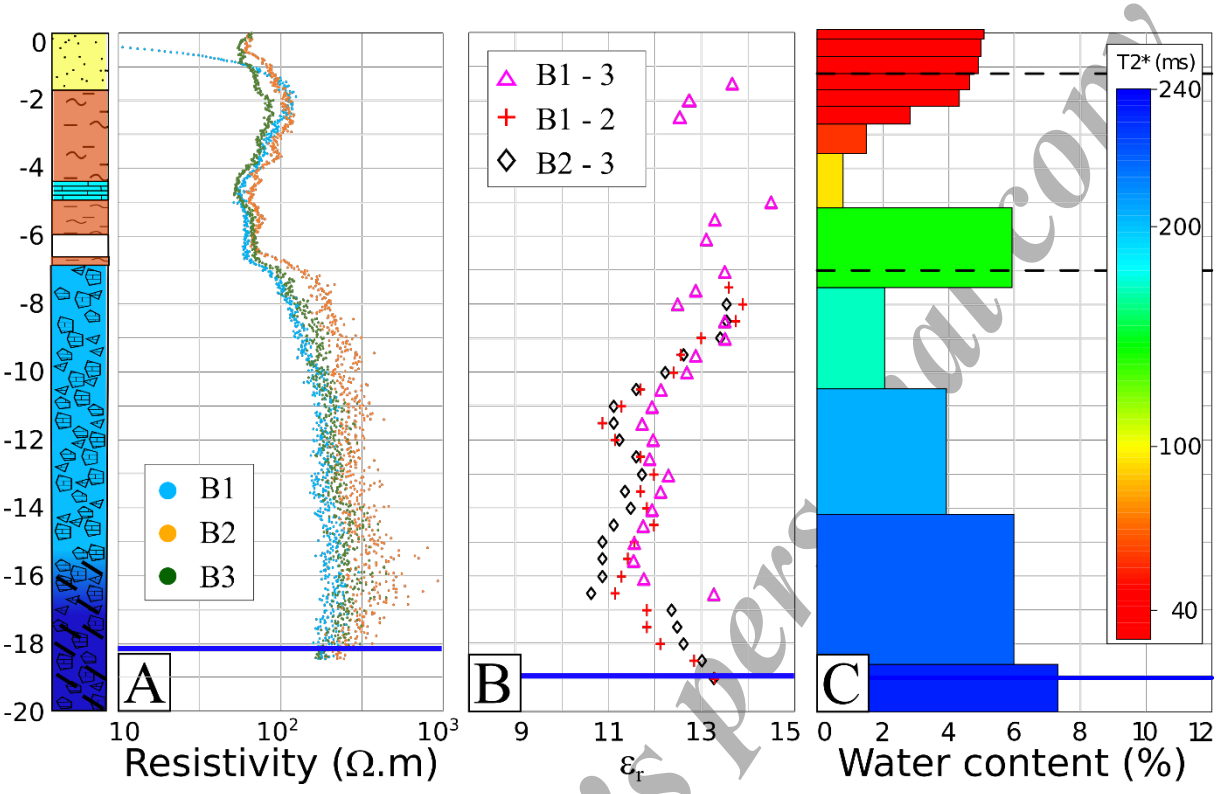

Figure 10. Geophysical profiles with respect to depth: A) electrical resistivity. B) cross-hole profile from GPR measurements. C) NMR water content and T2 (as defined by [41]) obtained from the NMR sounding [68]. On every figure the water table level is indicated by a blue line. On the left part a simplified lithological log is added (from Figure 2) with the soil formation followed by the incoherent limestone and the massive rock facies with an increase of fracturation from 15 m deep.*

The electric borehole sounding performed in March 2017 (Figure 8B and Figure 10A) shows an almost constant resistivity value from 1.5 to 7.0 m deep ranging from 40 to 60 Ω.m with a slight increase to 100 Ω.m at 2 m deep. Below this layer, the log gives an important accuracy about the distribution of the electric resistivity compared to the ERI with a high resistive layer ranging mostly from 100 to 300 Ω.m with some values going up all the way to 900 Ω.m between 15 and 17 m deep.

Radar profiles of the GPR monitoring campaign conducted on January 2019 are presented on Figure 10B. In our range of possible observations, we represent the results with ZOP cross-hole profiles between B1, 2 and 3. It appears that from 1 to 7 m deep, and due to significant wave attenuation (i.e. low resistive area), the GPR results are almost constant with a permittivity of 13.5. It decreases up to a permittivity of 11.5 at 11 m-deep and stay almost constant. We finally observe at 17 m-deep a jump of permittivity that could be due to the influence of the water table

revealing a capillary fringe. However, it cannot be assessed without further studies coupled to fracturation and macro-permeability measurements.

NMR 1D profile with T2* [40] is shown on Figure 10C for the loop sq20-4 (Figure 7A) with significant NMR water content variations. Between the surface and 5 m deep, NMR water content shows a decreasing trend from 5% to 1% with highest content observed for the soil. Between 5 and 8 m deep, water content increases rather abruptly from 1% up to 6%. Then, between 8 and 20 m deep, the NMR water content uniformly increases from 2% up to the water table where it reaches a value of 7%.

4. Discussion

4.1. Geophysics for microstructure and lithology

We compared here two different scales of observation for electrical and seismic measurements, to specify the O-ZNS lithology (laboratory scale of seismic data can be found in [37]).

Both ERI and seismic data, and lithological observations agree, highlighting three main layers including a silt loam soil, a heterogeneous incoherent and altered limestone, and a massive and altered/fractured limestone rock. Facies by facies we can add some specifications to these lithology and microstructures:

- **In the first two facies (from 0 to 1.5 and from 1.5 to 7.0 m deep)**, the almost constant borehole resistivity is interpreted in terms of interleafed materials with high content of clay and silt. This result is in good agreement with the direct core observations (Section 1.4). The transition at 1.5 m-deep between soil and incoherent limestone is not accurate between electric and seismic measurements showing the importance of coupling these data. Indeed, as seen on the seismic log extracted between B1 and 3 (Figure 9B orange curve), the transition is observed at 3 m deep. Although, this transition is highlighted by a slight ERI increase, but observed at 2 m-deep. The locally more important chargeability in A1 anomaly (<1.5 mV/V in the overall layer and up to 3 mV/V in A1 [68]) confirms the presence of clay in these overall facies. We also noted a slight decrease of electric resistivity in the lower part of this unit showing its higher clay content compared to the upper part. Here again we show the importance of comparing seismic data to any other as this anomaly is not observed on the seismic log extracted at this location (Figure 9B green curve)
- In the same layer, lithological log shown a thin layer of altered limestone rock around 4.5 m deep (Figure 2). It should imply a local increase of electric resistivity and seismic velocities that are, however, not observed. This could be due to the layer that is too thin or thus too

diffuse to be seen or, for the electrical data, to the method itself that is controlled by the less resistive surrounding material (A1 anomaly) that "hides" high resistive small inclusion [69].

- In the massive and altered limestone rock facies, from 7 to 20 m deep, a huge discrepancy (increasing after 15 m) was observed on the electrical log. This discrepancy is consistent with the variations observed on laboratory seismic measurements and during geomechanical tests [35]. It highlights an important degree of fracturation, becoming even more important after 15 m deep. In a companion laboratory study [39], the microcrack density has been estimated at around 0.3, with some local maximum up to 0.5 above 15 m deep. This is in good correlation with the observed fracturation on the core samples (Figure 4) and the lithological log (Figure 2). This increasing fracturation shown a limitation of the field seismic method. Indeed, it should be linked to a wave velocity decrease that cannot be observed by refraction methods. However, we still observe a slowdown of velocity increase with depth. On the other hand, we can see that electric resistivity data taken alone couldn't see this fracturation increase (except from its discrepancy). Indeed, the resistivity values are almost constant with no particular variations around 15-17 m-deep.
- Finally, for both ERI and seismic surface measurements, an increase was observed particularly between 17 and 20 m deep where silicified limestone rocks have been identified on direct core observations. However, due to the low resolution of these methods at that depth from surface investigations, no conclusion can be given regarding the extent of this silicified layer.

As a summary, 3D ERI and seismic surface methods have a lower resolution at greater depth but give an overview of the different lithological facies and spatial heterogeneities that brought us to revise the location of the well. The log measurements give us a better resolve of depth resistivity that match the direct core observations. Finally, we highlight the importance of coupling these two methods to depict both clay anomalies and fracturation increase that could be seen with a single method.

4.2. Hydrogeophysics: a powerful solution for monitoring the water content in the vadose zone

As part of the first characterizations carried out within the framework of the O-ZNS project, recent studies have focused on the simulation of water flow along the heterogeneous VZ of the Beauce limestone aquifer [33]. Ten undisturbed cored samples representative of the VZ facies (2-20 m deep) were extracted from B1 to 3. The hydraulic properties (water retention

and hydraulic conductivity) of these samples were determined in the laboratory [31]. A 23 m deep VZ profile composed of thirteen layers was reconstituted in HYDRUS-1D software [70] for B2. The hydrodynamic parameters of each layer were obtained using the RetC software [71] and by fitting the experimental hydraulic properties with the van Genuchten's expression (water retention curve) [72] and a statistical pore connection model (hydraulic conductivity curve) [73]. The simulation of water flow within the VZ profile was performed over a 54 years period (1966–2019) considering the meteorological and water level data. It allows us to compare our field geophysical measurements and interpretations to the water content values simulated at the same date (Figure 11).

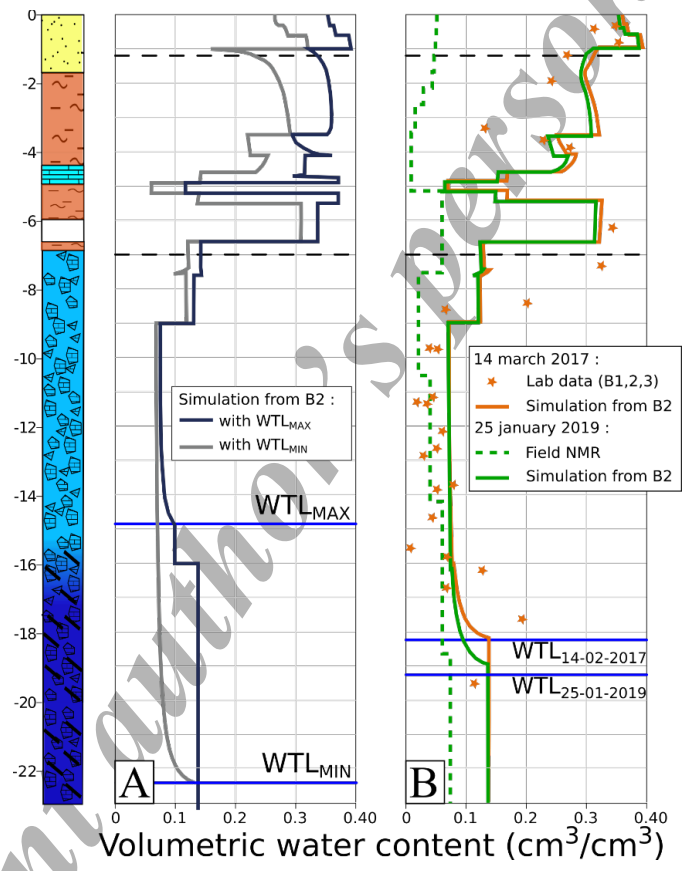

Figure 11. Volumetric water content values: (A) Simulated at the dates corresponding to the minimum and maximum water table levels. (B) Field NMR data compared to simulations at the same date.

Looking at the extreme water content variations between the minimum (WTL_{MIN} = -22.45 m on 26/08/1992) and maximum (WTL_{MAX} = -14.84 m on 18/05/2001) water table level, we observe that the water content of the deepest part of the VZ is relatively stable. Indeed, the most significant changes between the two profiles were observed between 0 and 7 m deep (> 0.10 cm^3/cm^3 and up to 0.23 cm^3/cm^3). Inversely, the least significant changes between the two profiles (< 0.05 cm^3/cm^3) were observed below 7 m (Figure 11A). This first observation asses the average geological interpretations highlighting the soil and the incoherent limestone facies

above 7 m deep followed by the massive and altered limestone rock facies down to the water table.

On Figure 11B, experimental water content measured on core samples in the laboratory were compared to simulations made at the same date [31]. This figure also compared the experimental NMR water content profile obtained from the surface NMR sounding sq20-4 made on 25/01/2019 (from Figure 10C) and water content simulated by HYDRUS-1D (based on hydraulic properties measured in the laboratory) at the same. At this stage of O-ZNS first characterization, we do not have the means to define petrophysical relations and thus link quantitively ERI and GPR to the water content (but it is currently under process). Still, we use the data presented in Figure 10 A and B to qualitatively improve our discussion, knowing that we have to stay careful because these data were not measured at the same date as the SNMR.

Between 0 and 7 m deep, the NMR results displayed much less water storage than the simulated profile. Although it has been shown that the model slightly overestimated laboratory experimental water content (Figure 11B orange results) [31], this difference is still important. It can be explained by the weak capability of NMR to detect water in materials with high proportions of clay and/or silt [7] that is largely present at these depths. Indeed, in this layer GPR data is not often measurable (Figure 10B) due to the low resistive area representative of a clayed zone. This is coherent with preliminary studies made within the framework of the O-ZNS project that have shown that the majority of the VZ materials located from 0 to 5 m deep had high proportions of clay and silt, ranging from 13 to 26 % and from 32 to 53 %, respectively [31].

In the thin sub-layer around 5 m deep, NMR results are slightly closer to those obtained with HYDRUS-1D. As highlighted by the visual examination of the undisturbed cored samples [31], this could be attributed to the calcareous sand intervals observed between 5 and 6 m deep and/or to the altered limestone rock observed at around 5 m deep in the VZ profile (Figure 2). Indeed, these geological facies displayed much lower clay and silt proportions than the other VZ materials allowing the NMR to detect more precisely their water content [6]. Note that, NMR results of the other loops demonstrated the same global variations of the water content along the VZ profile. It seems coherent with the ERI variations (Figure 10A) highlighting here a decrease in the resistivity (even so this comparison has to be considered carefully because these two measurements haven't been made at the same date). This observation could indicate the presence of a more clayey facies, but also the presence of a calcareous layer with low values of

water content. The second option is in good agreement with the simulated values of water content (Figure 11B orange results) and NMR results. Thus, our interpretation for this thin layer is the presence of a massive calcareous zone presenting a high porosity due to fracturation and alteration with low water content at the date of the measurements.

Between 8 and 23 m deep, NMR water content measured in the massive and altered limestone rock facies ranged from 0.020 to 0.085 cm^3/cm^3. These results were consistent with those obtained by Legchenko *et al.* [7] during surface NMR sounding conducted between 26/04/1999 and 15/03/2000 at a few hundred meters from O-ZNS study site. The simulated values were also relatively close, although always higher, than the experimental water content and SNMR results (Figure 11B). As observed by Legchenko *et al.* [7], and with this field data, it is worth noting that the NMR sounding did not allow to detect precisely the water table level (measured at -18.92 m on 25/01/2019) because of the limited resolution of the method or maybe because of the presence of a potential capillary fringe as seen by the GPR data.

5. Conclusion

Throughout this chapter, we proposed a multi-geophysical monitoring approach in order to characterize the lithological and petrophysical properties of a highly heterogeneous vadose zone of a vulnerable limestone aquifer.

Taken individually, electric, electromagnetic or seismic measurements are not able to fully describe the various sizes and scales of fractures and karsts present at different depths. Therefore, O-ZNS geophysical strategy relies on coupled methods. Altogether, geophysical imaging, made from the surface as well as in boreholes, makes it possible to obtain valuable information on lithology as well as about the variations of the water content within the VZ. Especially, SNMR preliminary results illustrates the impact of the presence of facies with low proportions of clay and silt on the variations in water content along the VZ. GPR highlights the possible presence of a capillary fringe and the water table level, with the increasing of permittivity observed from 17 m deep. ERI draws attention to the presence of layers with high proportions of clay and high water content identified between 4 and 7 m deep. Seismic measurement describes variation in the lithology with depth and also gives an estimation of the crack density at the laboratory scale.

With our first crossed interpretations, we have clearly shown that the results obtained with geophysical soundings can be coupled to laboratory hydraulic properties measurements and

numerical simulations, and lithological description made on undisturbed core samples. This comprehensive set of results lead to a significantly enhancement of possible interpretations. However, further studies are still needed for quantitatively linking the measured geophysical parameters to petrophysical and transport properties of the vadose zone. Ongoing work is focused on the joint inversion of data obtained through multiple surface and borehole geophysical soundings (NMR, GPR, ERI, Seismic, and Gravimetry) conducted in August 2020. In addition, it is planned to carry out laboratory investigations to accurately apply Topp and Archie's laws to quantitatively describe the water content from the already presented GPR and electric data [74-76]. Then, added to fracture and connected karst imagery from the seismic data, it is finally expected to obtain the overall in-situ permeability. Furthermore, larger scale investigations based on the O-ZNS well and surrounding boreholes will ensure complementary scales of observation and couplings of methods to reduce uncertainties and better image the VZ heterogeneities. To do so, it is planned to compare the surface well imagery (acquired during the well digging) to our multi-geophysical methods. The comparison of this whole set of data between them and with the hydrogeological measurements conducted in parallel should improve the estimation of the variations of the water content through the whole porosity (matrix and fractures) of the VZ. This will help for the characterization of the transport properties of its highly heterogeneous facies by building on 3D multiphase reactive transport models.

Acknowledgments

This research work was conducted within the framework of the O-ZNS project which is part of PIVOTS project. We gratefully acknowledge the financial support provided by the Région Centre-Val de Loire (ARD 2020 program and CPER 2015 -2020) and the French Ministry of Higher Education and Research (CPER 2015 -2020 and public service to BRGM). This is also co-funded by European Union with the European Regional Development Fund (FEDER). Finally, this research work is co-funded by the Labex VOLTAIRE (ANR-10-LABX-100-01). Authors are also thankful for the help of K. Moreau and B. Brigaud from Université Paris Saclay, S. Andrieu and E. Husson from the BRGM for the characterization of rock facies, L. Bodet, R. Guérin and CRITEX for the seismic acquisition, A. Bitri from the BRGM for the seismic inversion, J.-M. Baltassat and S. Ammor from the BRGM for the NMR acquisition and inversion, T. Jouen (ISTO) and J.-C. Gourry (BRGM) for the ERT acquisition and inversion, SEMM Logging for the geophysical logs, IRIS Instrument, Geosciences Montpellier and NMR Services Australia for the equipment loan.

References

[1] D. Stephens, “Vadose zone hydrology,” *CRC pres*s, 1995

[2] B. Arora, D. Dwivedi, B. Faybishenko, R. B. Jana and M. Wainwright, “Understanding and Predicting Vadose Zone Processes," *Reactive Transport in Natural and Engineered Systems*, 85, 303-328, 2019

[3] B. Abbar, A. Isch, K. Michel, H. Vincent, P. Abbasimaedeh and M. Azaroual, “Fiber optic sensors for environmental monitoring: state of the art and application in heterogeneous karstic limestone vadose zone of an agricultural field - Beauce Aquifer (O-ZNS), Orleans, France,” in “Instrumentation and Measurement Technologies for Water Cycle Management,” Chapter II.2

[4] K. Chalikakis, V. Plagnes, R. Guerin, R. Valois and F. Bosch, "Contribution of geophysical methods to karst-system exploration: an overview," *Hydrogeology Journal,* 19(6), 1169, 2011

[5] P. B. Lamb and D. R. Londhe, "Seismic behaviour of soft first storey," *IOSR Journal of Mechanical and Civil Engineering*, 2278-1684, 2012

[6] S. Falzone, J. Robinson and L. Slater, "Characterization and monitoring of porous media with electrical imaging: a review," *Transport in Porous Media*, 130(1), 251-276, 2019

[7] A. V. Legchenko, J.-M. Baltassat, C. Duwig, M. Boucher, J.-F. Girard, A. Soruco, A. Beauce, F. Mathieu, C. Legout, M. Descloitres and F. A. G. Patricia, "Time-lapse magnetic resonance sounding measurements for numerical modeling of water flow in variably saturated media," *Journal of Applied Geophysics*, 175, 103984, 2020

[8] J. Keskinen, A. Klotzche, M. C. Looms, J. Moreau, J. van der Kruk, K. Holliger, L. Stemmerik and L. Nielsen, "Full-waveform inversion of Crosshole GPR data: Implications for porosity estimation in chalk," *Journal of Applied Geophysics*, 140, 102-116, 2017

[9] C. Champollion, S. Deville, J. Chéry, E. Doerflinger, N. Le Moigne, R. Bayer, P. Vernant and N. Mazzilli, "Estimating epikarst water storage by time-lapse surface-to-depth gravity measurements," *Hydrology and Earth System Sciences*, 22(7), 3825-3839, 2018

[10] K. Vozoff and D. L. B. Jupp, "Joint inversion of geophysical data," *Geophysical Journal of the Royal Astronomical Society*, 42, 977-991, 1975

[11] N. Linde and J. Doetsch, "Joint inversion in hydrogeophysics and near surface geophysics," in “Integrated Imaging of the Earth: Theory and Applications”, *John Wiley & Sons*, 119-135, 2016

[12] L. A. Gallardao, S. L. Fontes, M. A. Meju, M. P. Buonora and P. P. de Lugao, "Robust geophysical integration through structure-coupled joint inversion and multispectral fusion of seismic reflection,

magnetotelluric, magnetic, and gravity images: Example from Santos Basin, offshore Brazil," *Geophysics*, 77(5), B237–B251, 2012

[13] J. Carcione, B. Ursin and J. Nordskag, "Cross-property relations between electrical conductivity and the seismic velocity of rocks," *Geophysics*, 72(5), 193-204, 2007

[14] K. Davis, Y. Li and M. Batzle, "Time-lapse gravity monitoring: A systematic 4D approach with application to aquifer storage and recovery," *Geophysics*, 73(6), WA61-WA69, 2008

[15] J. Doetsch, H. Krietsch, C. Schmelzbach, M. Jalali, V. Gischig, L. Villiger, F. Amann and H. Maurer, "Characterizing a decametre-scale granitic reservoir using ground-penetrating radar and seismic methods," *Solid Earth*, 11(4), 1441-1455, 2020

[16] T. Lochbühler, J. Doetsch, R. Brauchler and N. Linde, "Structure-coupled joint inversion of geophysical and hydrological data," *Geophysics*, 78(3), ID1-ID14, 2013

[17] R. Cassidy, J.-C. Comte, J. Nitsche, C. Wilson, R. Flynn and U. Ofterdinger, "Combining multi-scale geophysical techniques for robust hydro-structural characterisation in catchments underlain by hard rock in post-glacial regions," *Journal of hydrology*, 517, 715-731, 2014

[18] N. Linde, P. Renard, T. Mukerji and J. Caers, "Geological realism in hydrogeological and geophysical inverse modeling: A review," *Advances in Water Resources*, 86, 86-101, 2015

[19] D. Grana, "Joint facies and reservoir properties inversion Dario," *Geophysics*, 83(3), M15-M24, 2018

[20] N. Linde, A. Binley, A. Tryggvason, L. Pedersen and A. Revil, "Improved hydrogeophysical characterization using joint inversion of cross-hole electrical resistance and ground-penetrating radar traveltime data," *Water Resources Research*, 42(12), 2006

[21] A. Shahin, M. Myers and L. hathon, "Global optimization to retrieve borehole-derived petrophysical properties of carbonates," *Geophysics*, 85(3), D75-D82, 2020

[22] B. Heincke, M. Jegen, M. Moorkamp, R. W. Hobbs and J. Chen, "An adaptive coupling strategy for joint inversions that use petrophysical information as constraints," *Journal of Applied Geophysics*, 136, 279-297, 2017

[23] D. Colombo and D. Rovetta, "Coupling strategies in multiparameter geophysical joint inversion," *Geophysical Journal International*, 215(2), 1171-1184, 2018

[24] F. Miotti, A. Zerilli, P. T. L. Menezes, J. L. S. Crepaldi and A. R. Viana, "A new petrophysical joint inversion workflow : Advancing on reservoir's characterization challenges," *Interpretation*, 6(3), SG33-SG39, 2018

[25] C. Jordi, J. Doetsch, T. Günther, C. Schmelzbach, H. Maurer and J. O. A. Robertsson, "Structural joint inversion on irregular meshes," *Geophysical Journal International*, 220(3), 1995-2008, 2020

[26] A.A. Monaghan, B. O Dochartaigh, F. Fordyce, S. Loveless, D. Entwisle, M. Quinn, K. Smith, R. Ellen, S. Arkley, T. Kearsey, S.D.G. Campbell, M. Fellgett and I. Mosca, "UKGEOS: Glasgow Geothermal Energy Research Field Site (GGERFS): initial summary of the geological platform," 2017

[27] H.R. Bogena, C. Montzka, J.A. Huisman, A. Graf, M. Schmidt, M. Stockinger, C. Von Hebel, H.J. Hendricks-Franssen, J. Van Der Kruk, W. Tappe, A. Lücke, R. Baatz, R. Bol, J. Groh, T. Pütz, J. Jakobi, R. Kunkel, J. Sorg and H. Vereecken, "The TERENO-Rur hydrological observatory: A multiscale multi-compartment research platform for the advancement of hydrological science," *Vadose Zone Journal*, 17(1), 1-22, 2018

[28] S. Liu, X. Li, Z. Xu, T. Che, Q. Xiao, M. Ma, L. Qinhuo, J. Rui, G. Jianwen, W. Liangxu, W. Weizhen, Q. Yuan, L. Hongyi, X. Tongren, R. Youhua, H. Xiaoli, S. Shengjin, Z. Zhongli, T. Junlei, Z. Yang and R. Zhiguo, "The Heihe Integrated Observatory Network: A basin-scale land surface processes observatory in China," *Vadose Zone Journal*, 17(1), 1-21, 2018

[29] H.R. Bogena, T. White, O. Bour, X. Li, and K.H. Jensen, "Toward better understanding of terrestrial processes through long-term hydrological observatories," *Vadose Zone Journal,* 17(1), 2019

[30] L.A. Blazevic, L. Bodet, S. Pasquet, N. Linde, D. Jougnot, and L. Longuevergne, « Time-Lapse Seismic and Electrical Monitoring of the Vadose Zone during A Controlled Infiltration Experiment at the Ploemeur Hydrological Observatory, France," *Water*, 12(5), 1230, 2020

[31] C. Aldana, A. Isch, A. Bruand, M. Azaroual, and Y. Coquet, "Relationship between hydraulic properties and material features in a heterogeneous vadose zone of a vulnerable limestone aquifer," *Vadose Zone Journal*, e20127, 2021

[32] S. Ould Mohamed, A. Bruand, L. Bruckler, P. Bertuzzi, B. Guillet and L. Raison, "Estimating Long-Term Drainage at a Regional Scale Using a Deterministic Model," *Soil Science Society of America Journal*, 61(5), 1473-1482, 1997

[33] A. Isch, Y. Coquet, C. Aldana, A. Bruand and M. Azaroual, "Simulation of water flow and estimation of travail time through the heterogeneous vadose zone of a vunerable limestone aquifer based on laboratory hydraulic properties measurements," *Journal of Hydrology*, under review

[34] C. Aldana, "Etudes des propriétés de transfert de ka zone non saturée. Application aux calcaires aquitaniens de l'aqiufère de Beauce," *PhD thesis, Orleans'University*, 2019

[35] C. Mallet, J. Fortin, Y. Guéguen and F. Bouyer "Effective elastic properties of cracked solids: An experimental investigation," *International journal of fracture*, 182(2), 275-282, 2013

[36] C. Mallet, J. Fortin, Y. Guéguen and F. Bouyer," Evolution of the crack network in glass samples submitted to brittle creep conditions," *International Journal of Fracture*, 190(1-2), 111-124, 2014

[37] C. Mallet, A. Isch and M. Azaroual, "Heterogeneity and Fracturation characterization of the carbonate O-ZNS site through uniaxial and triaxial tests," *International journal of rock mechanics and mining sciences*, under review

[38] B. Fan, X. Liu, Q. Zhu, G. Qin, J. Li and L. Guo, "Exploring the interplay between infiltration dynamics and Critical Zone structures with multiscale geophysical imaging: A review," *Geoderma*, 374, 114431, 2020

[39] A. Binley, S. S. Hubbard, J. A. Huisman, A. Revil, D. A. Robinson, K. Singha and L. D. Slater, "The emergence of hydrogeophysics for improved understanding of subsurface processes over multiple scales," *Water resources research*, 51(6), 3837-3866, 2015

[40] A. V. Legchenko, "Magnetic resonance imaging for groundwater," *John Wiley & Sons*, 2013

[41] A. Behroozmand, K. Keating and E. Auken, "A review of the principles and applications of the NMR technique for near-surface characterization," *Surveys in geophysics*, 36(1), 27-85, 2015

[42] M. Müller-Petke and U. Yaramanci, "Resolution studies for Magnetic Resonance Sounding (MRS) using the singular value decomposition," *Journal of Applied Geophysics*, 66, 165-175, 2008

[43] T. Kremer, M. Müller-Petke, H. Michel, R. Dlugosch, T. Irons, T. Hermans and F. Nguyen, "Improving the accuracy of 1D surface nuclear magnetic resonance surveys using the multi-central-loop configuration," *Journal of Applied Geophysics*, 177, 104042, 2020

[44] J.-F. Girard, C. Jodry and P.-D. Matthey, "On-site characterization of the spatio-temporal structure of the noise for MRS measurements using a pair of eight-shape loops," *Journal of Applied Geophysics*, 178, 104075, 2019

[45] N. Mazzilli, M. Boucher, K. Chalikakis, A. V. Legchenko, H. Jourde and C. Champollion, "Contribution of magnetic resonance soundings for characterizing water storage in the unsaturated zone of karst aquifers," *Geophysics*, 81(4), WB49-WB61, 2016

[46] N. Mazzilli, K. Chalikakis, S. D. Carrière and A. V. Legchenko, "Surface nuclear magnetic resonance monitoring reveals karst unsaturated zone recharge dynamics during a rain event," *Water,* 12, 3183, 2020

[47] A. Gregory, "Fluid saturation effects on dynamic elastic properties of sedimentary rocks," *Geophysics*, 41(5), 896-921, 1976

[48] F. Haeni, "Application of seismic refraction methods in groundwater modeling studies in New England," *Geophysics*, 51(2), 236-249, 1986

[49] S. Pasquet, L. Bodet, P. Bergamo, C. Camerlynck, A. Dhemaied, N. Flipo, R. Guérin and F. Rejiba, "Contribution of seismic methods to hydrogeophysics," *Near Surface Geoscience 2015-21st European Meeting of Environmental and Engineering Geophysics*, 1, 1-5, 2015

[50] A. Révil, M. C. Karaoulis, T. C. Johnson and A. Kemna, "Review: Some low-frequency electrical methods for subsurface characterization and monitoring in hydrogeology," *Hydrogeology Journal*, 20(4), 617-658, 2012

[51] M. H. Loke, J. E. Chambers, D. F. Rucker, O. Kuras and P. B. Wilkinson, "Recent developments in the direct-current geoelectrical imaging method," *Journal of Applied Geophysics*, 95, 135-156, 2013

[52] P. Catarina, F. J. Alcalá, J. M. Carvalho and L. Ribeiro, "Current uses of ground penetrating radar in groundwater-dependent ecosystems research," *Science of the Total Environment*, 595, 868-885, 2017

[53] X. Liu, J. Chen, X. Cui, Q. Liu, X. Cao and X. Chen, "Measurement of soil water content using ground-penetrating radar: a review of current methods," *International Journal of Digital Earth*, 12(1), 95-118, 2019

[54] A. Revil, L. Cathles, S. Losh and J. Nunn, "Electrical conductivity in shaly sands with geophysical applications," *Journal of Geophysical Research*, 103(B10), 23925-23936, 1998

[55] D. Jougnot and A. Revil, "Thermal conductivity of unsaturated clay-rocks," *Hydrology Earth System Science*, 14, 91-98, 2010

[56] D. Michot, Y. Benderiter, A. Dorigny, B. Nicoullaud, D. King and A. Tabbagh, "Spatial and temporal monitoring of soil water content with an irrigated corn crop cover using surface electrical resistivity tomography," *Water resource Research*, 39(5), 2003

[57] A. Watlet, O. Kaufmann, A. Triantafyllou, A. Poulain, J. E. Chambers, P. I. Ledrum, P. B. Wilkinson, V. Hallet, Y. Quinif, M. Van Ruymbeke and M. Van Camp, "Imaging groundwater infiltration dynamics in the karst vadose zone with long-term ERT monitoring," *Hydrology and Earth System Sciences*, 22, 1563-1592, 2018

[58] P. Leroy, S. Li, D. Jougnot, A. Revil and Y. Wu, "Modeling the evolution of complex conductivity during calcite precipitation on glass beads," *Geophysical Journa International*, 209(1), 123-140, 2017

[59] J. Deparis, B. Fricout, D. Jongmans, T. Villemin, L. Effendiantz and A. Mathy, "Combined use of geophysical methods and remote techniques for characterizing the fracture network of a potentially unstable cliff site (the 'Roche du Midi', Vecors massif, France)," *Journal of Geophysics and Engineering*, 5(2), 147-157, 2008

[60] S.D. Carrière, K. Chalikakis, G. Sénéchal, C. Danquigny, and C. Emblanch, “Combining Electrical Resistivity Tomography and Ground Penetrating Radar to study geological structuring of karst Unsaturated Zone,” *Journal of Applied Geophysics*, 94, 31–41, 2013

[61] M. Lubczynski and J. Roy, "Magnetic resonance sounding: new method for ground water assessment," *Groundwater*, 42(2), 291-303, 2004

[62] G. T. Schuster and A. Quintus-Bosz, "Wavepath eikonal traveltime inversion: Theory," *Geophysics*, 58(9), 1314-1323, 1993

[63] S. R. Rohdewald, "Interpretation of first-arrival travel times with wavepath eikonal traveltime inversion and wavefront refraction method," *Symposium on the Application of Geophysics to Engineering and Environmental Problems*, 31-38, 2011

[64] F. C. Lin, M. H. Ritzwoller and R. Snieder, "Eikonal tomography: surface wave tomography by phase front tracking across a regional broad-band seismic array," *Geophysical Journal International*, 177(3), 1091-1110, 2009

[65] P. Hubral, M. Tygel and J. Schleicher, "Seismic image waves," *Geophysical Journal International*, 125(2), 431-442, 1996

[66] G. D. Team, "pyGIMLi tutorials," https://www.pygimli.org/_tutorials_auto/index.html. [Accessed 2020]

[67] B. Giroux, E. Gloaguen and M. Chouteau, " bh_tomo - A Matlab borehole georadar 2D tomography package," *Computers & Geosciences*, 33(1), 126-137, 2007

[68] C. Jodry, T. Jouen, A. Isch, J.-M. Baltassat, J. Deparis, G. Laurent, C. Mallet and M. Azaroual, "Geophysical imaging for the petrophysical properties characterization of a limestone heterogeneous vadose zone – beauce aquifer (france)," in *AGU Fall Meeting, San Fransisco, USA*, December 2019

[69] W. M. Telford, L. P. Geldart and R. E. Sheriff, "Applied geophysics," *Cambridge university press*, 1990

[70] J. Šimůnek, M. T. van Genuchten and M. Šejna, "Recent developments and applications of the HYDRUS computer software packages," *Vadose Zone Journal*, 7(15), 25, 2016

[71] M. van Genuchten, F. Leif and S. Yates, "The RETC code for quantifying hydraulic functions of unsaturated soils," *USEPA, Washington, DC*, 1991

[72] M. van Genuchten, "A closed-form equation for predicting the hydraulic conductivity of unsaturated soils," *Soil Science Society of America Journal*, 44(5), 892-898, 1980

[73] Y. Mualem, "A new model for predicting the hydraulic conductivity of unsaturated porous media," *Water Resources Research*, 12(3), 513-522, 1976

[74] G.E. Archie, "The electrical resistivity log as an aid in determining some reservoir characteristics," *Transactions of the AIME*, 146(01), 54–62,1942

[75] G.C. Topp, J.L. Davis, and A.P. Annan, "Electromagnetic determination of soil water content: measurements in coaxial transmission lines," *Water Resources Research*, 16(3), 574–582, 1980

[76] P.W.J. Glover, "Geophysical properties of the near surface Earth: electrical properties," in "Treatise on Geophysics," 11, 89-137, 2011